Long-chain alkylammonium organic–inorganic hybrid perovskite for high performance rechargeable aluminon-ion battery

Shu-Chi Wu [a,b,d,j,1], Zhengxun Lai [f,1], Ruoting Dong [f], Shin-Yi Tang [a,b,d,j,k], Kuangye Wang [a,b,d,j], Tzu-Yi Yang [a,b,d,j], Ying-Chun Shen [a,b,d,j], Hsiang-Ju Liao [a,b,d,j], Teng-Yu Su [a,b,d,j], Chiou-Ru Cheng [a,b,d,j], Yuanfei Ai [e], Yu-Ze Chen [c], Yi-Chung Wang [a,b,d,j], Ling Lee [a,b,d,j], Yi-Jen Yu [i], Johnny C. Ho [f,g,h,*], Yu-Lun Chueh [a,b,d,j,**]

[a] Department of Materials Science and Engineering, National Tsing Hua University, Hsinchu 30013, Taiwan
[b] Colleage of Semiconductor Research, National Tsing-Hua University, Hsinchu 30013, Taiwan
[c] Department of Materials Science and Engineering, National Cheng Kung University, Tainan 701, Taiwan
[d] Frontier Research Center on Fundamental and Applied Sciences of Matters, National Tsing Hua University, 30012 Hsinchu, Taiwan
[e] Dongguan University of Technology, Dongguan, Guangdong 523808, China
[f] Department of Materials Science and Engineering, City University of Hong Kong, Kowloon 999077, Hong Kong Special Administrative Region
[g] State Key Laboratory of Terahertz and Millimeter Waves, City University of Hong Kong, Kowloon 999077, Hong Kong Special Administrative Region
[h] Institute for Materials Chemistry and Engineering, Kyushu University, Fukuoka 816-8580, Japan
[i] Instrument Center, National Tsing Hua University, Hsinchu 30013, Taiwan
[j] Department of Physics, National Sun Yat-Sen University, Kaohsiung, 80424, Taiwan
[k] Semiconductor Research Center, Hon Hai Research Institute, Taipei 11492, Taiwan

ARTICLE INFO

ABSTRACT

Recent advances in the use of organic-inorganic hybrid perovskites have been investigated in a variety of applications, such as solar cells, photodetectors, light-emitting devices, and lasers, because of their outstanding semiconductor properties. Furthermore, the perovskite structure can host extrinsic elements, making it a promising candidate for battery applications. Previous studies have shown that organic-inorganic hybrid perovskites can be suitable anode materials for both lithium- and sodium-ion batteries. However, multivalent rechargeable batteries with perovskite materials have not yet been realized. Herein, we studied the electrochemical performance of three-dimensional ($CH_3NH_3PbI_3$ ($MAPbI_3$) and long-chain alkylammonium ($C_4H_9NH_3$)$_2$(CH_3NH_3)$_3Pb_4I_{13}$ ((iBA)$_2$(MA)$_3Pb_4I_{13}$) thin films as electrode materials for rechargeable Al-ion batteries. Our results showed that (iBA)$_2$(MA)$_3Pb_4I_{13}$ presented a specific capacity of 257 mAh g^{-1} at a current density of 0.1 A g^{-1} and delivered 108 mAh g^{-1} after 250 cycles at a current density of 0.3 A g^{-1} with a retention of as high as 91 %, demonstrating a crucial role of isobutyl amine ($C_4H_9NH_3$) due to the unique hydrogen-bonding interaction of isobutyl amine that hinders the shuttle effect of polyiodide. The results open a new direction for the use of organic–inorganic hybrid perovskites for new secondary aluminum ion batteries.

1. Introduction

Organic–inorganic hybrid perovskites have been widely studied owing to their variety of applications, such as in solar cells [1,2], photocatalytic hydrogen generation [3], photodetectors [4], X-ray detectors [5], light-emitting devices [6], lasers [7], and memory devices [8] attributable to their outstanding semiconductor properties. Previous studies have shown that organic-inorganic hybrid perovskites are fast ionic conductors with large diffusion coefficients, indicating that hybrid halide perovskite-based materials have great potential for a variety of electrochemical applications [9]. In 2015, Xia et al. demonstrated $CH_3NH_3PbBr_3$ as a Li-ion battery anode material, achieving a high

---

discharge capacity of 330 mAh g^{-1} and a stable capacity of ~200 mA h g^{-1} after the 200th cycle, which is approximately equal to that of a commercial graphite anode [10]. However, the energy storage mechanism remains unclear. Dawson et al. combined a computational–experimental study to examine Li ion intercalation and conversion mechanisms in CH$_3$NH$_3$PbBr$_3$ [11]. It is suggested that the conversion process with the production of CH$_3$NH$_3$Br, LiBr, and Pb metal, as opposed to Li-ion intercalation. In addition, Tathavadekar et al. reported that using low-dimensional hybrid perovskites, high reversible capacities of 646 and 315 mA h g^{-1} can be achieved for Li- and Na-ion batteries, respectively, owing to the low-dimensional hybrid perovskites exhibiting an open structure, which is beneficial for the rapid kinetics of ion accessibility [12]. Meanwhile, Ramirez et al. reported that 3D CH$_3$NH$_3$PbI$_{3-x}$Br$_x$ and 2D (CH$_3$NH$_3$)$_2$(CH$_3$(CH$_2$)$_2$NH$_3$)$_2$Pb$_3$Br$_{10}$ thin film as electrode for Li-ion batteries. The 3D hybrid perovskites exhibited large discharge capacities of 350–500 mA h g^{-1}, while charge capacities faded to 70–160 mA h g^{-1} in the first cycle, indicating other processes taking place during the Li intercalation. In contrast, the 2D hybrid perovskites with a layered structure delivered a capacity of ~375 mA h g^{-1} with 100 % reversibility of lithium insertion–extraction, suggesting that 2D layered structures are advantageous for reversible Li-ion storage [13]. Moreover, it was found that the mechanism of lithium insertion–extraction is accompanied by the alloying–dealloying process of the intermetallic Li$_x$Pb compounds. Recently, Wang *et al.* demonstrated that MAPbBr$_3$ composite electrodes exhibited excellent cyclic stability for more than 1000 cycles, which can be attributed to their small size, low defect concentration structure, and good interface charge transfer [14].

However, the safety (i.e., lithium dendrite formation) and potential price spike of lithium are debated. In terms of sustainable development, alternative battery technologies that have the advantages of higher abundance and lower cost are highly desirable, which may offer better safety features and higher energy density. Batteries based on multivalent metals with relatively high abundances in the Earth's crust, such as sodium, magnesium, and aluminum, have been considered to meet the future needs of large-scale energy storage [15]. To the best of our knowledge, multivalent rechargeable batteries with perovskite materials have not yet been realized. In this regard, we demonstrate for the first time the electrochemical performance of three-dimensional (3D) CH$_3$NH$_3$PbI$_3$ (MAPbI$_3$) and long-chain alkylammonium (C$_4$H$_9$NH$_3$)$_2$(CH$_3$NH$_3$)$_3$Pb$_4$I$_{13}$ ((*i*BA)$_2$(MA)$_3$Pb$_4$I$_{13}$) thin films as electrode materials for rechargeable Al-ion batteries. Compared with MAPbI$_3$, the (*i*BA)$_2$(MA)$_3$Pb$_4$I$_{13}$ yielded a specific capacity of 257 mAh g^{-1} at a current density of 0.1 A g^{-1} and delivered 108 mAh g^{-1} after 250 cycles at a current density of 0.3 A g^{-1} with retention of as high as 91 %, demonstrating the vital role of isobutyl amine (C$_4$H$_9$NH$_3$). The excellent performance can be attributed to the unique hydrogen-bonding interaction of isobutylamine, which effectively hindered the shuttle effect of polyiodide as confirmed by ex-situ FT-IR, Raman, X-ray photoelectron spectroscopy (XPS), ESI-MS, and density functional theory (DFT) calculations. Consequently, findings have shown that organic-inorganic hybrid perovskites are promising candidates for new secondary batteries.

2. Results and discussion

MAPbI$_3$, (*i*BA)$_2$(MA)$_3$Pb$_4$I$_{13}$, and PbI$_2$ electrodes were synthesized by a one-step electrodeposition method on a polytetrafluoroethylene (PTFE) coating carbon cloth, referred to as 3D long-chain alkylammonium (LCA) perovskites and PbI$_2$, respectively. The XRD results of LCA pervoskites, 3D pervoskites, PbI$_2$, and PTFE-coated carbon cloth are shown in Figs. 1a and S1. The diffraction peaks in Fig. 1a are fitted with the (111) and (220) peaks corresponding to LCA perovskites [16]. The FESEM images (Fig. 1b, Figs. S2-S4) reveal a uniform distribution of
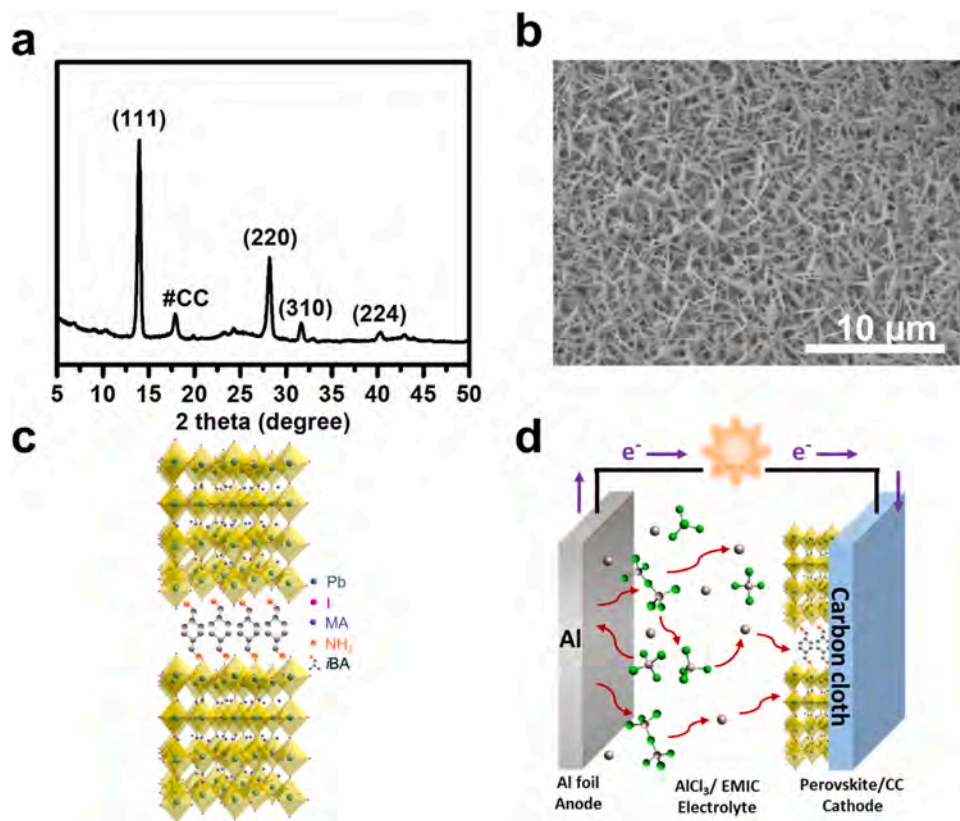
Fig. 1. Characterization and schematic of LCA perovskite/Al battery. (a) XRD pattern and (b) SEM image of LCA perovskite electrode, (c) schematic of LCA Perovskite structure, (d) schematic of LCA perovskite/Al battery.

fiber-like crystal structures on the PTFE coating carbon cloth, suggesting the chemical reactions performed in the precursor solutions and nucleated on the PTFE coating during the film formation, which prolongs crystal growth and promotes simultaneous nucleation [12,13,17], providing good adhesion at the interface between carbon cloth and perovskite layer [18]. The corresponding element mapping images in Figs. S2-S4 and Table S1 list the lead and iodine ratios of three electrodes, which are in good agreement with chemical formula. LCA perovskites were used in this work because they can self-assemble into layered structures where inorganic layers of corner-sharing $[PbI_6]^{4-}$ octahedra are confined between interdigitating bilayers of organic cations through indirect cross-linking by hydrogen bonding or van der Waals forces (Fig. 1c)[19]. A schematic representation of the LCA perovskite/Al battery is presented in Fig. 1d.

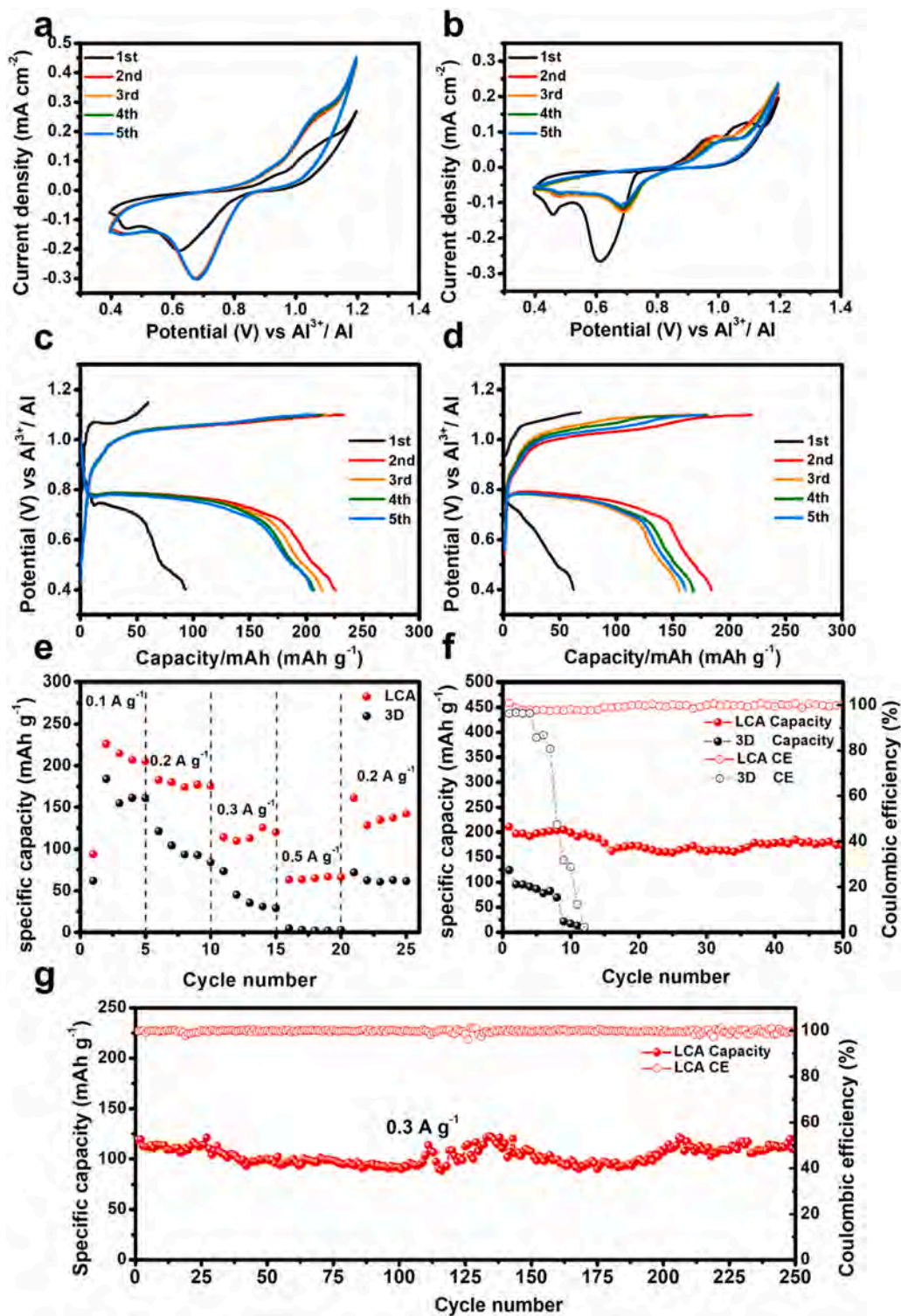**Fig. 2.** Electrochemical performance of LCA perovskite/Al battery Cyclic voltammogram of the (a) LCA and (b) 3D perovskite/Al batteries; Galvanostatic curves (0.1 A g^{-1}) of (c) LCA perovskite and (d) 3D perovskite (e) rate capability of 3D and LCA perovskite/Al battery; (f) cycling performance (0.2 A g^{-1}) of LCA and 3D perovskite and (g) long cycling performance (0.3 A g^{-1}) of LCA perovskite/Al battery.

Cyclic voltammetry tests were conducted on LCA perovskite/Al batteries with LCA perovskite as the working electrode and Al foil as the counter and reference electrodes, respectively, under ionic liquid electrolytes at a scan rate of 0.1 mV s^{-1}. To prevent the decomposition of perovskite and maintain Coulombic efficiency, the cut-off voltage of the cell was set to the potential range of 1.2–0.4 V (vs. Al) as shown in Figs. S5a and S5b. Fig. S5a presents the potential range from 1.5 to 0.4 V (vs. Al) and the current slope at high voltage range and minor cathodic peak at low voltage, indicating polyiodide I$_5^-$ formation during the cycling process and leading to the irreversible reaction in further cycles [20]. Fig. S5b presents the potential range from 1.1 to 0.01 V (vs. Al) and shows that there are two pairs of reduction/oxidation peaks at 0.3/0.48 and 0.68/1.1 V. The major pair of peaks at 0.3/0.48 can be assigned to the Pb/Pb^{2+} redox pair [21–24] and the minor pair of peaks at 0.68/1.1 V corresponds to the I$_3^-$/I$^-$ redox chemistry [20,25]. However, the curve of the Pb/Pb^{2+} redox pair becomes unstable at the further scan and disappears at the fifth cycle, implying that the lead may dissolve in the ionic liquid electrolyte at a lower potential range (> 0.4 V) [21,24,26]. As a result, the range of operating voltage needs to be effectively controlled. During the initial scan, the cathodic peak of LCA pervoskite and 3D pervoskite were located at about 0.45 V and 0.46 V, respectively, which can be attributed to perovskite structure decomposition and the formation of the SEI layer[13,27,28] (Fig. 2a and b). In further cyclic voltammetry (CV) curves of LCA perovskite and 3D perovskite, there were one pair of reduction/oxidation peaks at 0.7/1.1 V and 0.67/1.1 V.These peaks can be ascribed to one-step redox reaction associated with the reversible conversion reaction (corresponding analysis see the following energy storage mechanism section), corresponding to the valence change of iodine from I$_3^-$ to I$^-$ [20,25]. Moreover, the CV curves displayed similar shapes after the first cycle, suggesting the high reversibility of the discharge-charge process of the LCA perovskite/Al batteries. The battery performances of the LCA pervoskite/Al and 3D perovskite/Al batteries with ionic liquids are shown in Fig. 2c and d. The galvanostatic curves in Fig. 2c reveal that the LCA perovskite delivers a discharging specific capacity of 226 mAh g^{-1} at a current density of 0.1 A g^{-1} with a discharging plateau at ~0.8 V vs. Al [20,25]. In contrast, the 3D perovskite delivers a discharging specific capacity of 180 mAh g^{-1} at a current density of 0.1 A g^{-1}. Furthermore, the charge-discharge plateaus in these two batteries correlate with the redox peaks in the respective CV curves. Fig. S6 shows the corresponding cyclic voltammetry curves of the PbI$_2$ as the cathode at a scan rate of 0.1 mV s^{-1} and the charge-discharge profiles at a current density of 0.1 A g^{-1}. The PbI$_2$ /Al battery delivered a higher initial discharge capacity of ~275 mAh g^{-1} at a specific current of 0.1 A g^{-1} (Fig. S6a) because of its high intrinsic electron conductivity, leading to a high initial discharge capacity (Fig. S6b). However, the rapid capacity decay and some noise cyclic voltammetry curves can be observed for the subsequent cycles owing to the loss of active materials by the dissolution effect of PbI$_2$. Rate capability tests were conducted at current densities from 0.1 to 0.5 A g^{-1} with cycling for 5 cycles at each current density as shown in Figs. 2e and S7. Clearly, the LCA perovskite produced a higher capacity and higher coulombic efficiency than the 3D perovskite at each current density. For the LCA perovskite/Al battery, average reversible capacities of 214, 177, 116, and 65 mAh g^{-1} were obtained at current densities of 0.1, 0.2, 0.3, and 0.5 A g^{-1}, respectively, suggesting that the isobutyl amine effectively blocked the diffusion of polyiodide and enhanced the reaction kinetics at high current densities. In contrast, the 3D perovskite/Al battery exhibited lower kinetics performance, and only 35 % and 19 % capacity were retained at 0.2 and 0.3 A g^{-1}, respectively. Stability tests were performed in these two batteries at a current density of 0.2 A g^{-1} as shown in Fig. 2f. Distinctly, the LCA perovskite/Al battery showed an initial discharge capacity of 201 mAh g^{-1} and slightly decayed to 173 mAh g^{-1} within 50 cycles. However, the 3D perovskite/Al battery delivered an initial discharge capacity of 104 mAh g^{-1} and could only reversibly charge and discharge for less than 12 cycles. Fig. S8 shows the corresponding charge-discharge profiles at

0.2 A g^{-1} at 8–12 cycles. Obviously, the 3D perovskite/Al battery delivered rapid capacity decay and some noise charge-discharge profiles during the subsequent cycles because the 3D perovskite can be dissolved in the ionic liquid [29,30]. Furthermore, the SEM-EDS mapping images of the 3D perovskite cathode after the 12th cycle are shown in Fig. S9. Note that the surface of the cathode is smooth and the Pb and I elements vanished, confirming the dissolution of 3D perovskite materials and exposure of the substrate, which is in good agreement with the charge-discharge profiles at subsequent cycles. Note that Al and Cl single were from the ionic liquid electrolyte, and C and F elements were from the PTFE-coated carbon cloth substrate. In addition, the LCA perovskite/Al battery exhibited a high coulombic efficiency of 98 % over 50 cycles, whereas that of the 3D perovskite/Al battery is only 80 %. The relatively low stability and Coulombic efficiency of the 3D perovskite/Al battery may arise from the dissolution effect of the 3D perovskite. The electrochemical impedance spectra of LCA perovskite and 3D perovskite measured at an open-circuit voltage of ~0.8 V are shown in Figs. S10 and S11. Figs. S10a and S11a show the entire frequency range of LCA perovskite and 3D perovskite, respectively. Figs. S10b and S11b focus on the high-frequency range of LCA perovskite and 3D perovskite, respectively. Fig. S12 shows the corresponding equivalent circuit model, with which R_s represents the resistance of the electrolyte, R_{ct} and CPE2 are the charge-transfer resistance and capacitance of the electrode/electrolyte interface, and CPE1 is used to simulate the diffusive behavior in the low-frequency range. The results of the circuit models are listed in Tables S2 and S3. Note that the R_{ct} of the 3D perovskite electrodes gradually increases from 6.63 Ω (0th cycle) to 151 Ω (11th cycle). The higher R_{ct} of the 3D perovskite electrodes may result from the PTFE coating, indicating the dissolution effect of the 3D perovskite and the exposure of the substrate. In contrast, the R_{ct} of LCA perovskite electrodes decreases from 35.02 Ω (0th cycle) to 14.19 Ω (5th cycle). The lower R_{ct} of the LCA perovskite electrodes may result from the LCA perovskite structure becoming non-crystalline during cycling. Notably, long-chain alkylammonium cations act as insulation block layers, disturbing charge carrier transfer between phases [31,32], leading to the higher R_{ct} of LCA perovskite electrodes in the initial state. However, the LCA perovskite structure became non-crystalline during cycling, indicating that the structure was recomposited and the charge transport properties were improved. Moreover, after continuous cycling for 50 cycles, the R_{ct} of LCA perovskite electrodes increases from 14.19 Ω (5th cycle) to 23.27 Ω (50th cycle), indicating that the non-crystalline of LCA perovskite was stable during the further cycling. Moreover, a long-term stability test was performed in an LCA perovskite/Al battery under a current density of 0.3 A g^{-1}, and the results are shown in Fig. 2g. The LCA perovskite/Al battery displayed excellent cycling stability with a remarkable capacity of 108 mAh g^{-1} and a Coulombic efficiency of ~91 % after 250 cycles, suggesting that the excellent reversibility of the LCA perovskite effectively blocked the diffusion of polyiodide and enhanced the battery stability. Table S4 shows a comparison of the conversion mechanism of the cathode material in a nonaqueous aluminum ion battery and various reported cycle capacities. Compared with sulfide and halide-based materials, our LCA perovskite electrode exhibited good cycling for 250 cycles.

The peak current (I_p in A) of LCA perovskite and 3D perovskite electrode increases with an increase in the scan rate from 0.3 to 0.5 mV s^{-1} (Fig. 3a and b). As the scanning rate increases, a pair of redox peaks can be observed due to the polarization effect at high scan rates (Fig. 3c and d). All cathodic and anodic peaks for the LCA perovskite and 3D perovskite electrodes displayed a linear relationship with the square root of scanning rates, for which the Randles–Sevcik equation can be applied to estimate Al^{3+} ion diffusion (D_{Al}^{3+} in cm^2/s) given by $\frac{I_p}{\sqrt{v}} = 2.69 \times 10^5 n^{1.5} A \sqrt{D_{Al^{3+}}} C_{Al^{3+}}$, for which v is the potential scan rate (V s^{-1}), n is the charge transfer number, A is the geometric area of the active electrode (cm^2), and C_{Al}^{3+} is the concentration of Al ions in the electrolyte (mol/cm^3). The higher D_{Al}^{3+} suggests that the electrode
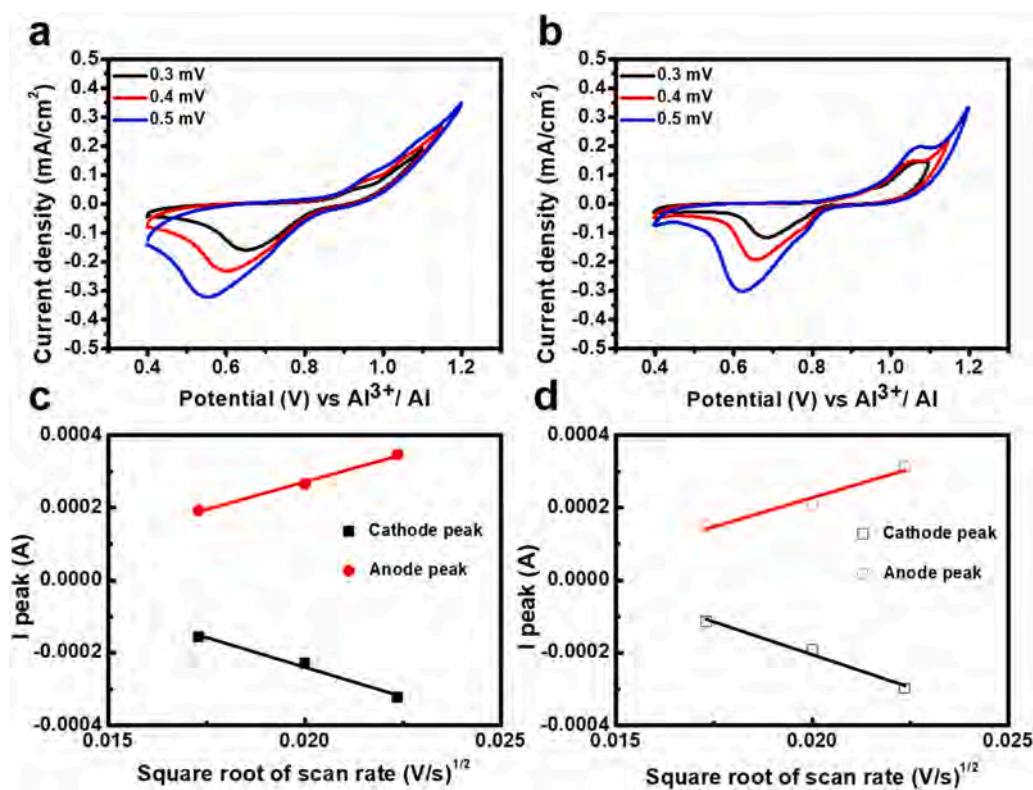
Fig. 3. Kinetic studies of the LCA perovskite/Al battery. Cyclic voltammograms curves of (a) LCA Perovskite electrode and (b) 3D perovskite electrode at various scan rates. Peak current for (c) LCA Perovskite electrode and (d) 3D perovskite electrode vs. the square root of the scan rates.

provided relatively strong aluminum ion transfer capability [33,34]. The LCA perovskite electrode ($D_{Al}^{3+} = 1.5 \times 10^{-18}$–$4.3 \times 10^{-18}$ cm^2 s^{-1}) demonstrated superior diffusion kinetics compared to the 3D perovskite electrode ($D_{Al}^{3+} = 7.7 \times 10^{-19}$–$3.4 \times 10^{-18}$ cm^2 s^{-1}), implying that the LCA perovskite effectively hindered the shuttle effect of polyiodide and improved battery performance. Notably, these values are comparable to the Al ion diffusion coefficient in sulfide-based materials [33,35]. D_{Al}^{3+} for batteries with two electrodes and sulfide-based materials from previous reports are listed in Table S5. In contrast, the limited aluminum-ion transfer in the 3D perovskite control causes unstable and low-scan peaks, which also show the degradation of the electrochemical reversibility during continuous scanning.

To clarify the possible reaction mechanism in the LCA perovskite/Al battery, various ex-situ measurements, such as XRD, XPS, FTIR spectroscopy, Raman spectroscopy, and ESI-MS, were conducted. The XRD spectra of the LCA perovskite cathode after the discharge and charge processes are shown in Fig. 4a. The main diffraction peaks of the LCA perovskite electrode at 14° and 28.1° correspond to (110) and (220) planes, respectively, and the peak at 18.1° can be assigned to carbon cloth (Fig. S13). Interestingly, at a discharge of 0.4 V, the main peak of the LCA perovskite almost completely disappeared, while the new diffraction peaks formed at 12.55° can be ascribed to the formation of PbI$_2$ (JCPDS no.73-0591) [36]. Moreover, the additional small peaks at 10° and 30° can be assigned to methylamine, and those at 11° and 19° can be assigned to isobutylamine (Fig. S13). At a charge of 1.2 V, the weak signals of methylamine and isobutylamine still existed, but the peak PbI$_2$ vanished. Furthermore, peaks of the LCA perovskite cathode after the 5th discharge state and the charged state almost disappeared, suggesting that the LCA perovskite structure was decomposed and became non-crystalline during the further discharge-charging process [13,27,28] (Fig. S14). To shed light on the mechanism during the discharge-charging process, ex-situ Raman spectroscopy was used to examine the formation of non-crystalline compounds during the charge–discharge processes at the 5th cycle as shown in Fig. 4b. In the initial

state, the two main peaks of the LCA perovskite located at 87 and 136 cm^{-1} can be assigned to the stretching of the Pb–I bonds and the vibrations of the amine cations, respectively [37,38]. At the discharged state of 0.4 V, these two main peaks became negligible, indicating that the LCA perovskite structure was consumed, matching the results of ex-situ XRD discharge states. Simultaneously, two peaks appeared at 110 and 143 cm^{-1}, which can be assigned to the symmetric stretching mode and asymmetric stretching for I$_3^-$ [20,25], respectively. As the battery charged to 1.2 V, the peak intensity of I$_3^-$ increases corresponding to the transformation of I$^-$ to I$_3^-$ under the charge state. Compared to the discharge state, the opposite reaction occurs in the charge state, confirming the I$_3^-$/I$^-$ redox chemistry observation in this system. Notably, in the charge state, a new broad peak at 225 cm^{-1} can be assigned to PbCl$_3^-$ owing to PbI$_2$, which may react with the Lewis acidic chloroaluminate melt [26]. The corresponding reference Raman spectra are listed in Table S6. Moreover, ESI-MS was applied to the electrolyte for further cycles to further confirm these species, as shown in Fig. S15. The negative ESI mass spectra show peaks at $m/z = 128$ and 312, corresponding to species I$^-$ and PbCl$_3^-$, respectively, which are in good agreement with the ex-situ Raman results. To further clarify the important role of hydrogen-bonding interaction from the amine in the perovskite cathode, ex-situ FTIR spectroscopy was carried out at the 5th cycle, and the spectra are shown in Fig. 4c and S16. The peak located at approximately 3000–3300 cm^{-1} is assigned to the stretching vibration of the amine. Under the discharge state, the peak of half-width gradually increases and a significant blue shift occurs.[4] Under the charge state, the enlargement of the blue shift increases. Considering the ex-situ XRD results, the perovskite cathode was expected to be decomposed during the first discharge-charge process and the decomposed product included methylamine and isobutylamine [13,27,28]. Considering that two amine molecules are polar and I$_3^-$ is relatively polar. The adsorbent composed of these molecules would strongly interact with I$_3^-$. These phenomena resulted from the formation of hydrogen bonds between the amine and I$_3^-$, indicating that the LCA perovskite effectively hindered
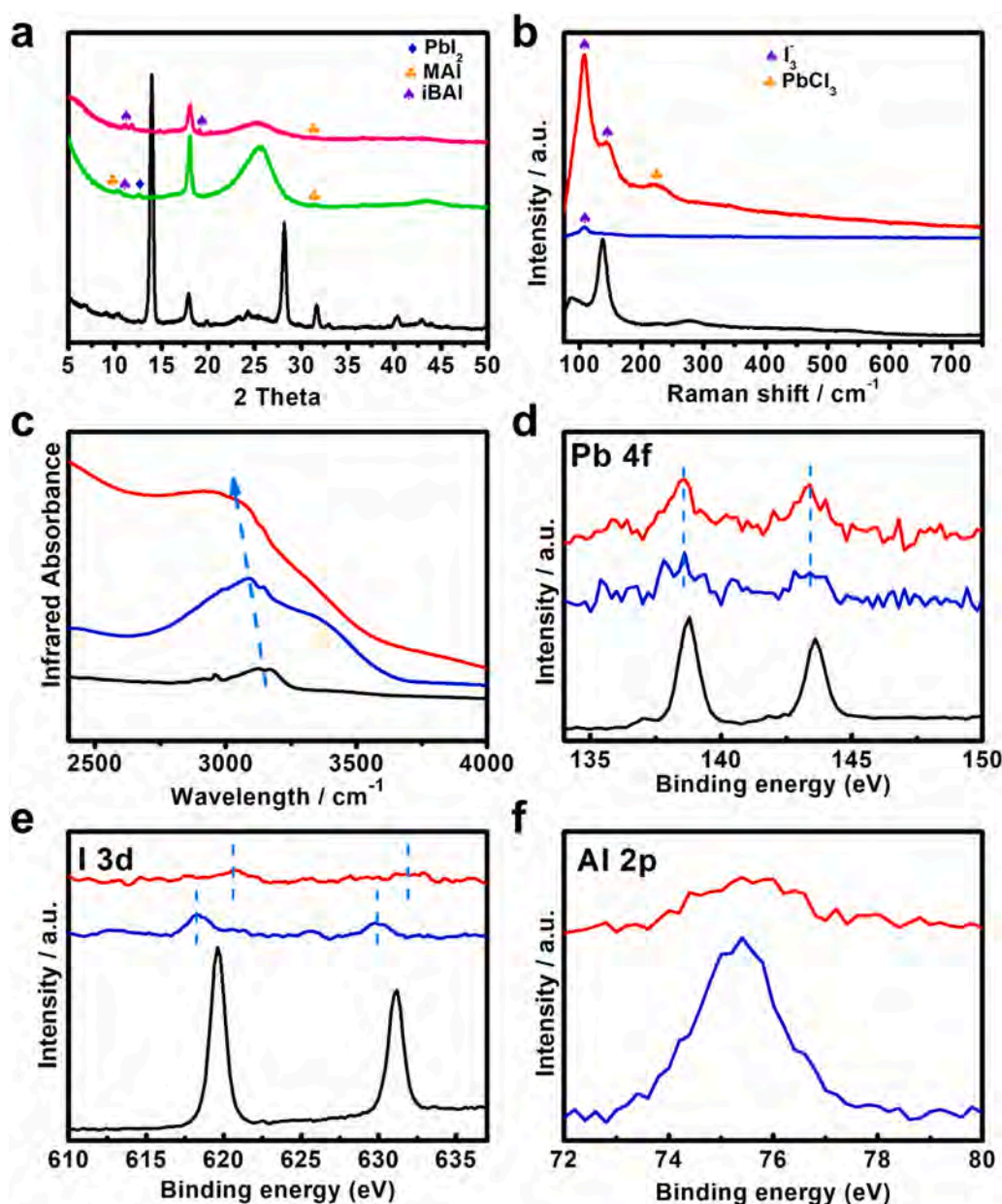
Fig. 4. Ex-situ measurements of the LCA perovskite/Al battery. (a) XRD, **(b)** FTIR, and **(c)** Raman of LCA Perovskite electrode at different states after 5 cycles. **(c)** XPS Pb 4 f and **(d)** I 3d spectra of LCA Perovskite electrode at different states after 5 cycles, respectively. Black profile: Pristine LCA perovskite electrode; Green profile: 1st discharge to 0.4 V; Pink profile: 1st charge to 1.2 V; Blue profile: 5th discharge to 0.4 V; Red profile: 5th charge to 1.2 V.
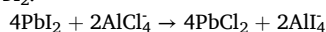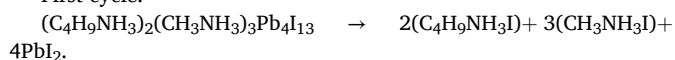
the shuttle effect of polyiodide and improved the battery performance. XPS was used to further analyze the chemical state of the LCA perovskites during the charge–discharge process as shown in Fig. 4d to f. Fig. 4d shows the Pb-4 f XPS spectra of the LCA perovskites at specific states. For the pristine LCA perovskites electrode, Pb-4 f spectra display two peaks at ~138.8 (Pb-4 $f_{7/2}$) and ~143.6 eV (Pb-4 $f_{5/2}$), which are in full agreement with values previously reported [39]. As the battery discharged and charged, two main peaks of Pb 4 f peak were observed at 138.6 (Pb-4 $f_{7/2}$) and 143.5 eV (Pb-4 $f_{5/2}$) in these two samples, which were attributed to the the PbI_2 that may react with the Lewis acidic chloroaluminate melt [26], resulting in the formation of $PbCl_2$ or $PbCl_3$ [40], matching ex-situ Raman and ESI-MS results. Meanwhile, XPS spectra of I-3d were also analyzed at different states and displayed in Fig. 4e. The I-3d spectra of the pristine LCA perovskites electrode show two peaks at binding energies of 619.5 eV (I $-3d_{5/2}$) and 631.0 eV ((I $-3d_{3/2}$). As the battery was discharged, the I $3d_{5/2}$ peak shifts to 618.3 eV, confirming the formation of AlI_4^- as the discharged product

[41–45]. Under the charge state, the I $3d_{5/2}$ peak shifts back to 620.0 eV, suggesting the oxidation of AlI_4^- back to I_3^-, indicating that the process is highly reversible [20,25]. Furthermore, the XPS spectra of Al-2p were applied at the discharge and charge states as shown in Fig. 4f. Under the discharge state, the Al 2p XPS peak at 75.0 eV could be assigned to the Al 2p binding energy of aluminum halide, further confirming the existence of AlI_4^- [41,42,44,45]. As the battery charged, the inconspicuous peak of Al 2p confirmed that AlI_4^- was reversibly oxidized to I_3^-. As shown in Figs. S17-S18 and Table S7 for the images of the LCA perovskite cathode and the atomic composition, respectively, there were some changes on the electrode, but Pb and I were still in the composition after the 5th discharge and 5th charge processes. Notably, the compositions of the iodine in the charge state were higher than those in the discharge state, indicating the formation of I_3^-, matching the results of ex-situ FTIR, Raman, and XPS. SEM images of the Al foil anode for the LCA perovskite battery and 3D perovskite battery were also obtained after the cycling processes as shown in Figs. S19 and S20, respectively. Clearly, the Al

anode for the LCA perovskite battery showed rugged spots on the surface after the cycling processes, which could be attributed to various degrees of corrosion caused by the active $Al_2Cl_7^-$ anions in the electrolytes [20]. Although the Al anode was polished using emery paper to remove the passive layer, some oxygen still existed on the fresh aluminum surface (Fig. S19). Note that the Al anode for the 3D perovskite battery was covered with dense cycling products (Fig. S20). However, some Pb and I signals can be observed on the Al anode surface, suggesting the dissolution effect of the 3D perovskite. The LCA perovskite battery effectively prohibits the dissolution of lead and iodine, indicating that Pb centers remain in the matrix of the isobutylamine molecules during the charge-discharge process according to the composition difference on the anode surface. This phenomenon is also beneficial to the matrix of isobutylamine molecules, providing a strain-absorbing environment to avoid the detachment of lead from the electrode during the cycling process [12].
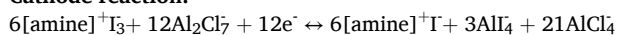
To further reveal the interaction between amine and I_3^-, we employed first-principle calculations to compare the adsorption energies of methylamine and isobutylamine (Fig. 5). The adsorption energy was defined as E(ads) = E(total)–(E(surf)+E(I_3^-)), where E(ads), E(total), E (surf), and E(I_3^-) are the adsorption energies of I_3^- on various surfaces, total energy of the adsorption state, energy of the surface, and energy of the mono I_3^- molecule, respectively. The more negative the E(ads) is, the stronger the adsorption ability of the material is to avoid the shuttle effect of polyiodide, leading to good cycling performance. The details of the calculation are provided in Tables S8 and S9, and the calculated E (ads) values of the different adsorption systems are listed in Table S10. The E(ads) of isobutylamine-bound I_3^- was calculated to be − 9.31 kcal/ mol, which is higher than the E(ads) of methylamine-bound I_3^- (−7.52 kcal/mol). The free I_3^- typically presents a proximal linear configuration with a bond angle of 180° but I_3^- undergoes slight structural distortion upon binding with amine molecules, leading to a decrease in the bond angle($\angle$I–I–I). It can also be observed that the bond angle ($\angle$I–I–I) with isobutylamine was calculated to be ~178.8°, which is lower than the bond angle ($\angle$I–I–I) with methylamine (~179.3 °) (Table S8). This implies the structural distortion of I_3^-, which suggests a strong interaction between isobutylamine and I_3^- [46], leading to relatively good cycling performance. Combining the ex-situ XRD, XPS, Raman, FTIR, SEM-EDS and ESI-MS results, we propose the following mechanism for rechargeable LCA perovskite/Al batteries:

First cycle:

$(C_4H_9NH_3)_2(CH_3NH_3)_3Pb_4I_{13}$ → $2(C_4H_9NH_3I)$+ $3(CH_3NH_3I)$+ $4PbI_2$.

$4PbI_2 + 2AlCl_4^- → 4PbCl_2 + 2AlI_4^-$

Subsequent cycles:

Cathode reaction:

$6[amine]^+I_3$+ $12Al_2Cl_7^-$ + $12e^-$ ↔ $6[amine]^+I^-$ + $3AlI_4^-$ + $21AlCl_4^-$

$[amine]^+ = C_4H_9NH_3^+$ and $CH_3NH_3^+$.

Anode reaction:

$4Al + 28 AlCl_4^- ↔ 16Al_2Cl_7^- + 12 e^-$

3. Conclusion

In summary, for the first time, we successfully fabricated thin film electrodes of 3D (MAPbI$_3$) and long-chain alkylammonium (iBA)$_2$(-MA)$_3$Pb$_4$I$_{13}$) organic–inorganic hybrid perovskite thin films as electrode materials for rechargeable Al-ion batteries; the (iBA)$_2$(MA)$_3$Pb$_4$I$_{13}$ electrode yielded a specific capacity of 257 mAh g^{-1} at a current density of 0.1 A g^{-1} and delivered 108 mAh g^{-1} after 250 cycles at a current density of 0.3 A g^{-1} with a retention of as high as 91 %, indicating a long cycling stability. Compared with MAPbI$_3$, (iBA)$_2$(MA)$_3$Pb$_4$I$_{13}$ exhibited higher initial capacities, better reversibility, better high-rate capabilities, and higher diffusion coefficient (D_{Al}^{3+}), demonstrating the vital role of isobutylamine (C$_4$H$_9$NH$_3$). The excellent performance can be attributed to the unique hydrogen-bonding interaction of isobutylamine, which effectively hindered the shuttle effect of polyiodide, as confirmed by ex-situ FT-IR, Raman, XPS, ESI-MS, and DFT calculations. Furthermore, the matrix of isobutylamine molecules provided a strain-absorbing environment to avoid the detachment of lead from the electrode during cycling. These findings shed light on the mechanism of multivalent rechargeable batteries with organic-inorganic hybrid perovskite materials and will inform the design of novel organic-inorganic hybrid perovskite-based batteries with high capacities and long cycle lives.

4. Experimental section

4.1. Materials

The raw materials, PbI$_2$, C$_4$H$_9$NH$_3$I ($iBAI$), CH$_3$NH$_3$I (MAI), AlCl$_3$, and 1-ethyl-3-methylimidazolium chloride (EMIC), were commercially available from Alfa Aesar. Polytetrafluoroethylene (PTFE) coated carbon cloth was purchased from CeTech Co. Ltd.

4.2. Synthesis of perovskites

The synthesis of perovskite was performed using a one-step spin-coating method reported previously [16]. For the synthesis of CH$_3$NH$_3$PbI$_3$, the precursor solutions were prepared by dissolving PbI$_2$ and MAI at a molar ratio of 1:1 in dimethyl formamide (DMF). For the synthesis of (iBA)$_2$(MA)$_3$Pb$_4$I$_{13}$, the precursor solutions were prepared by dissolving PbI$_2$, $iBAI$, and MAI at a molar ratio of 4:2:3 in dimethyl formamide (DMF). Both precursor solutions were stirred overnight at room temperature. The PTFE-coated carbon cloth substrates were first treated by UV–ozone for 15 min to improve their hydrophilia before the spin-coated process. Then, 50 μL of the precursor solution was spin-coated on the PTFE-coated carbon cloth at 3000 rpm for 30 s, followed by thermal annealing at 100 °C for 15 min for full crystallization
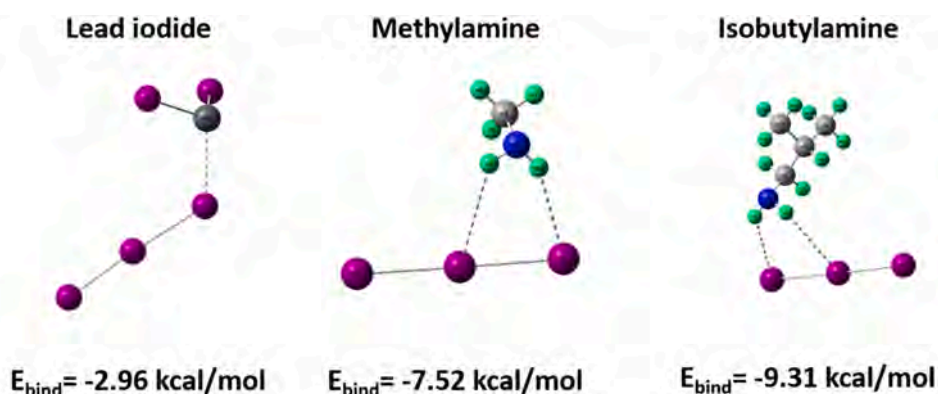

Fig. 5. DFT calculation I$_3$ absorption energy of (a) lead iodide, (b) methylamine, and (c) isobutylamine.

of the samples. The specific areal loading of the active material was determined by growing perovskites on 1×1 cm^2 substrates and dividing the mass difference by area, giving approximately 0.5 mg cm^{-2}. All the samples were prepared in an Ar-filled glove box ([O$_2$] < 0.1 ppm, [H$_2$O] < 0.1 ppm).

4.3. Preparation of EMIC(1-ethyl-3-methylimidazolium chloride)-AlCl$_3$ electrolyte

Anhydrous AlCl$_3$ (Alfa Aesar, ≥99 %) was slowly added to 1-ethyl-3-methylimidazolium chloride (EMIC, >98 %, Io-Li-Tec) under stirring for ~0.5 h to form a homogeneous liquid. All the electrolytes were prepared in an Ar-filled glove box ([O$_2$] < 0.1 ppm, [H$_2$O] < 0.1 ppm).

4.4. Material characterization

The morphologies and microstructures of the samples were investigated using field-emission scanning electron microscopy (FESEM; Hitachi FE-SEM SU8010). A micro-Raman spectroscopy instrument (LabRAM HR800, Horiba) equipped with a green laser (532 nm) was used to identify the phase and examine the quality of the sample. The binding energies of Pb, I, and Al were examined by XPS using a PHI 5000 Versaprobe II. The resolution of the Fourier transform infrared (FTIR) spectra is 2 cm^{-1} with a scan number of 200. ESI ionization time-of-flight mass spectroscopy (ESI-TOF MS) measurements were performed by a JMS-T100LP4G (JEOL) mass spectrometer equipped with an ESI source. The ESI measurement conditions included a needle voltage of 2000 kV, an orifice voltage of 1 V at 300 V, a ring lens voltage of 10 V, and a spray temperature of 250 °C.

4.5. Electrochemical measurements

A piece of 1×1 cm^2 perovskite on a carbon cloth was directly used as the cathode, and a piece of 1.5×1.5 cm^2 Al foil (0.25 mm, 99.99 %, Sigma) was used as the anode. In addition, the glass fiber was used as the separator (ADVANTEC, GC-50), and the Ni ears were used as the current collector with a mixture of anhydrous aluminum chloride and 1-ethyl-3-methylimidazolium chloride at a mole ratio of 1.3:1 (1.5 mL for each pouch) used as the IL electrolyte. Finally, a 5×10 cm^2 aluminum laminated film pouch cell was used to assemble the Al-ion batteries in an Ar-filled glove box ([O$_2$] < 0.1 ppm, [H$_2$O] < 0.1 ppm). Electrochemical tests of the Al-ion batteries were carried out on an electrochemical workstation (Bio-logic, VPS), and galvanostatic and cycling measurements were conducted using a LAND battery testing system.

4.6. Computational details

The geometric structures of monomers and complex compounds were optimized with the B3LYP/(6–311 +G**, Lanl2DZ) level (in which, 6–311 +g** basic set for C/H/N atoms, and Lanl2DZ basic set for I and Pb atoms) using the Gaussian 09 package, and the frequency calculations were carried out at the same level [46–49]. All the structures had no imaginary frequency and were proven to be the local minimums on the potential energy surface by frequency calculations, indicating that structures obtained were stable that can be used in the following exploration. Based on the optimized structures, their single-point energies were calculated using the MP2/(6–311 ++G**, Lanl2DZ) level (in which the 6–311 +g** basic set for C/H/N atoms, and Lanl2DZ basic set for I and Pb atoms). The adsorption energy of I$_3^-$ on various surfaces was calculated by $E_{ads} = E_{total} - \left(E_{surf} + E_{I_3^-} \right)$ where E_{ads} is the adsorption energy of I$_3^-$ on various surfaces, E_{total} is the total energy of the absorption state, E_{surf} is the energy of the surface, and $E_{I_3^-}$ is the energy of the mono I$_3^-$ molecule.

CRediT authorship contribution statement

S. C. W., Z. X. L., J. C. H., and **Y. L. C.** conceived and coordinated the study. **S. C. W., Z. X. L., R. T. D., S. Y. T., K. Y. W., T. Y. Y., Y. C. S., H. J. L., T. Y. S., C. R. C., Y. F. A., Y. Z. C., Y. C. W.,Y. J. Y.,** and **L. L.** conducted the experiments and performed the data analysis. **S. C. W.** and **Z. X. L.** plotted the curves and figures. **S. C. W.** and **Y. L. C.** provided the theoretical guidance. All authors discussed the results and commented on the manuscript. **S. C. W., Z. X. L., J. C. H,** and **Y. L. C.** prepared the manuscript draft with contributions from all coauthors.

Declaration of Competing Interest

The authors declare that they have no known competing financial interests or personal relationships that could have appeared to influence the work reported in this paper.

Data availability

Data will be made available on request.

Appendix A. Supporting information

Supplementary data associated with this article can be found in the online version at doi:10.1016/j.nanoen.2023.108273.

References

[1] Q. Chen, H. Zhou, Z. Hong, S. Luo, H.-S. Duan, H.-H. Wang, Y. Liu, G. Li, Y. Yang, J. Am. Chem. Soc. 136 (2014) 622–625.

[2] J. Burschka, N. Pellet, S.-J. Moon, R. Humphry-Baker, P. Gao, M.K. Nazeeruddin, M. Grätzel, Nature 499 (2013) 316–319.

[3] S. Park, W.J. Chang, C.W. Lee, S. Park, H.-Y. Ahn, K.T. Nam, Nat. Energy 2 (2016) 16185.

[4] Y. Guo, C. Liu, H. Tanaka, E. Nakamura, J. Phys. Chem. Lett. 6 (2015) 535–539.

[5] Q. Chen, J. Wu, X. Ou, B. Huang, J. Almutlaq, A.A. Zhumekenov, X. Guan, S. Han, L. Liang, Z. Yi, J. Li, X. Xie, Y. Wang, Y. Li, D. Fan, D.B.L. Teh, A.H. All, O. F. Mohammed, O.M. Bakr, T. Wu, M. Bettinelli, H. Yang, W. Huang, X. Liu, Nature 561 (2018) 88–93.

[6] Z.-K. Tan, R.S. Moghaddam, M.L. Lai, P. Docampo, R. Higler, F. Deschler, M. Price, A. Sadhanala, L.M. Pazos, D. Credgington, F. Hanusch, T. Bein, H.J. Snaith, R. H. Friend, Nat. Nanotechnol. 9 (2014) 687–692.

[7] H. Zhu, Y. Fu, F. Meng, X. Wu, Z. Gong, Q. Ding, M.V. Gustafsson, M.T. Trinh, S. Jin, X.Y. Zhu, Nat. Mater. 14 (2015) 636–642.

[8] E.J. Yoo, M. Lyu, J.-H. Yun, C.J. Kang, Y.J. Choi, L. Wang, Adv. Mater. 27 (2015) 6170–6175.

[9] N. Vicente, G. Garcia-Belmonte, Adv. Energy Mater. 7 (2017), 1700710.

[10] H.-R. Xia, W.-T. Sun, L.-M. Peng, Chem. Commun. 51 (2015) 13787–13790.

[11] J.A. Dawson, A.J. Naylor, C. Eames, M. Roberts, W. Zhang, H.J. Snaith, P.G. Bruce, M.S. Islam, ACS Energy Lett. 2 (2017) 1818–1824.

[12] M. Tathavadekar, S. Krishnamurthy, A. Banerjee, S. Nagane, Y. Gawli, A. Suryawanshi, S. Bhat, D. Puthusseri, A.D. Mohite, S. Ogale, J. Mater. Chem. A 5 (2017) 18634–18642.

[13] D. Ramirez, Y. Suto, N.C. Rosero-Navarro, A. Miura, K. Tadanaga, F. Jaramillo, Inorg. Chem. 57 (2018) 4181–4188.

[14] Q. Wang, T. Yang, H. Wang, J. Zhang, X. Guo, Z. Yang, S. Lu, W. Qin, CrystEngComm 21 (2019) 1048–1059.

[15] Y. Liang, H. Dong, D. Aurbach, Y. Yao, Nat. Energy 5 (2020) 646–656.

[16] R. Dong, C. Lan, X. Xu, X. Liang, X. Hu, D. Li, Z. Zhou, L. Shu, S. Yip, C. Li, S.-W. Tsang, J.C. Ho, ACS Appl. Mater. Interfaces 10 (2018) 19019–19026.

[17] P.-W. Liang, C.-C. Chueh, X.-K. Xin, F. Zuo, S.T. Williams, C.-Y. Liao, A.K.Y. Jen, Adv. Energy Mater. 5 (2015), 1400960.

[18] N.A. Nadege Ouedraogo, M. Yang, C. He, Y. Chen, X. Zhang, H. Yan, C.B. Han, Y. Zhang, Sustain. Energy Fuels 4 (2020) 4257–4263.

[19] C.C. Stoumpos, D.H. Cao, D.J. Clark, J. Young, J.M. Rondinelli, J.I. Jang, J. T. Hupp, M.G. Kanatzidis, Chem. Mater. 28 (2016) 2852–2867.

[20] S. Zhang, X. Tan, Z. Meng, H. Tian, F. Xu, W.-Q. Han, J. Mater. Chem. A 6 (2018) 9984–9996.
[21] F.-X. Wang, G.-B. Pan, Y.-D. Liu, Y. Xiao, Chem. Phys. Lett. 488 (2010) 112–115.
[22] L. Anicai, I. Sin, O. Brincoveanu, S. Costovici, A. Cotarta, A. Cojocaru, M. Enachescu, T. Visan, Appl. Surf. Sci. 475 (2019) 803–812.
[23] Y. Katayama, R. Fukui, T. Miura, J. Electrochem. Soc. 160 (2013) D251–D255.
[24] T.J. Simons, A.K. Pearson, S.J. Pas, D.R. MacFarlane, Electrochim. Acta 174 (2015) 712–720.
[25] H. Tian, S. Zhang, Z. Meng, W. He, W.-Q. Han, ACS Energy Lett. 2 (2017) 1170–1176.
[26] F. Coleman, G. Feng, R.W. Murphy, P. Nockemann, K.R. Seddon, M. Swadźba-Kwaśny, Dalton Trans. 42 (2013) 5025–5035.
[27] N. Tewari, S.B. Shivarudraiah, J.E. Halpert, Nano Lett. 21 (2021) 5578–5585.
[28] S. Ahmad, C. George, D.J. Beesley, J.J. Baumberg, M. De Volder, Nano Lett. 18 (2018) 1856–1862.
[29] L. Chao, T. Niu, H. Gu, Y. Yang, Q. Wei, Y. Xia, W. Hui, S. Zuo, Z. Zhu, C. Pei, X. Li, J. Zhang, J. Fang, G. Xing, H. Li, X. Huang, X. Gao, C. Ran, L. Song, L. Fu, Y. Chen, W. Huang, Research 2020 (2020), 2616345.
[30] L. Chao, T. Niu, Y. Xia, Y. Chen, W. Huang, Acc. Mater. Res. 2 (2021) 1059–1070.
[31] H. Tsai, W. Nie, J.-C. Blancon, C.C. Stoumpos, R. Asadpour, B. Harutyunyan, A.J. Neukirch, R. Verduzco, J.J. Crochet, S. Tretiak, L. Pedesseau, J. Even, M.A. Alam, G. Gupta, J. Lou, P.M. Ajayan, M.J. Bedzyk, M.G. Kanatzidis, A.D. Mohite, Nature 536 (2016) 312–316.
[32] D. Cortecchia, S. Neutzner, A.R. Srimath Kandada, E. Mosconi, D. Meggiolaro, F. De Angelis, C. Soci, A. Petrozza, J. Am. Chem. Soc. 139 (2017) 39–42.
[33] L. Geng, J.P. Scheifers, C. Fu, J. Zhang, B.P.T. Fokwa, J. Guo, ACS Appl. Mater. Interfaces 9 (2017) 21251–21257.
[34] S.-C. Wu, Y.-H. Huang, C.-R. Liao, S.-Y. Tang, T.-Y. Yang, Y.-C. Wang, Y.-J. Yu, T.-P. Perng, Y.-L. Chueh, Nano Energy 90 (2021), 106590.
[35] H. Li, H. Yang, Z. Sun, Y. Shi, H.-M. Cheng, F. Li, Nano Energy 56 (2019) 100–108.
[36] B.P. Dhamaniya, P. Chhillar, A. Kumar, K. Chandratre, S. Mahato, K.P. Ganesan, S.K. Pathak, A.C.S. Omega 5 (2020) 31180–31191.
[37] Z. Liang, S. Zhang, X. Xu, N. Wang, J. Wang, X. Wang, Z. Bi, G. Xu, N. Yuan, J. Ding, RSC Adv. 5 (2015) 60562–60569.
[38] M. Ledinský, P. Löper, B. Niesen, J. Holovský, S.-J. Moon, J.-H. Yum, S. De Wolf, A. Fejfar, C. Ballif, J. Phys. Chem. Lett. 6 (2015) 401–406.
[39] N. Li, C. Cheng, H. Wei, H. Liu, X. Li, W. Li, L. Wang, RSC Adv. 7 (2017) 42105–42112.
[40] T.-W. Ng, C.-Y. Chan, M.-F. Lo, Z.Q. Guan, C.-S. Lee, J. Mater. Chem. A 3 (2015) 9081–9085.
[41] X. Zhang, C. Liu, Y. Ma, Y. Shen, H. Li, R. Chen, Y. Mai, Sol. Energy 148 (2017) 70–77.
[42] L. Yu, F.-C. Liu, Z.-W. Fu, Electrochim. Acta 54 (2009) 2818–2822.
[43] L. Ma, M.S. Kim, L.A. Archer, Chem. Mater. 29 (2017) 4181–4189.
[44] G.M. Begun, C.R. Boston, G. Torsi, G. Mamantov, Inorg. Chem. 10 (1971) 886–889.
[45] A. Manteghetti, A. Potier, Spectrochim. Acta Part A Mol. Spectrosc. 38 (1982) 141–148.
[46] J. Wang, Z. Li, Y. Wang, C. Wei, K. Ai, L. Lu, Mater. Horiz. 6 (2019) 1517–1525.
[47] M.W. Schmidt, K.K. Baldridge, J.A. Boatz, S.T. Elbert, M.S. Gordon, J.H. Jensen, S. Koseki, N. Matsunaga, K.A. Nguyen, S. Su, T.L. Windus, M. Dupuis, J.A. Montgomery Jr, J. Comput. Chem. 14 (1993) 1347–1363.
[48] A.D. Becke, J. Chem. Phys. 88 (1988) 2547–2553.
[49] J.P. Perdew, K. Burke, M. Ernzerhof, Phys. Rev. Lett. 77 (1996) 3865–3868.

Zhengxun Lai received his BSc in applied physics and MS degrees in material physics and chemistry from Tianjin University in 2016 and 2019. Currently, he is a Ph.D. candidate majoring in material science and engineering at City University of Hong Kong. His research interests are focused on the halide perovskites electronic and photoelectric devices.

Routing Dong received her BSc and MS degrees from South China Normal University in 2013 and 2016. After that, she started to pursue her Ph.D. degree at City University of Hong Kong and graduated in 2019. Her research interest is quasi-2D halide perovskites-based photodetectors.

Shin-Yi Tang received her BS degree in material science and engineering from National Tsing Hua University in 2016. After that, she started to pursue her PhD degree and is currently a PhD candidate in the department of material science and engineering, National Tsing Hua University. Her research interests include the synthesis and sensing applications of TMDC materials with various nanostructures and heterojunctions.

Kuangye Wang is a Ph.D. candidate in Department of Materials Science and Engineering, National Tsing Hua University, Taiwan. His research interests include the synthesis of 2D materials, hydrogen evolution reaction and gas sensing devices.

Tzu-Yi Yang is a Ph.D. candidate in Department of Materials Science and Engineering, National Tsing Hua University, Taiwan. His research interests include direct growth, fundamental characterizations, and optoelectronic applications of two-dimensional materials and energy harvesting by Cu(In,Ga)Se2 solar cells.

Shu-Chi Wu has received his Ph.D. degree in material science and engineering from National Tsing Hua University, Taiwan in 2022. After that, he is currently a postdoctoral researcher in the department of chemistry, Stanford University, United States. His research interests include transition metal dichalcogenide synthesis and battery application (including lithium, sodium, magnesium, aluminum and zinc ion battery).

Ying-Chun Shen received her BS degree in material science and engineering from National Tsing Hua University in 2018. After that, she started to pursue her Ph.D. degree and is currently a Ph.D. candidate in the department of material science and engineering, National Tsing Hua University. Her research interests include the synthesis and transfer of 2D materials and improvement of RRAM devices.

Yu-Ze Chen received his Ph.D. degree from Department of Materials Science and Engineering, National Tsing Hua University. Currently, he is an Assistant Professor in Dept. of Materials Science and Engineering at the National Cheng Kung University. His research interests focus on the synthesis of low-dimensional materials and the application for energy harvesting. Details can be found at: https://yzchenlab.wixsite.com/website

Hsiang-Ju Liao received her bachelor's degree from Department of Chemistry in National Taiwan Normal University in 2016. She worked as a research assistant in Prof. Di-Yan Wang's lab in Tunghai University from 2016 to 2017. After that, she received her master's degree from Department of Materials Science and Engineering in National Tsing-Hua University, Taiwan. Her research interests focus on dual ion battery and zinc ion battery application.

Yi-Chung Wang received his Ph.D. degree from Department of Materials Science and Engineering, National Tsing Hua University. Experienced Postdoctoral Researcher with a demonstrated history of working in the renewable energy industry. Skilled in thin-film solar cells, nanofabrication, optical simulation. Research professional with a Ph.D. focused in Materials Science and Engineering from National Tsing Hua University.

Teng-Yu Su received his Ph.D. degree from Department of Materials Science and Engineering, National Tsing Hua University in 2019. His research interests include fabrication of resistive switching memory (ReRAM), synthesis TMDC materials with electrical/sensing application, the optical/electrical characterization

Ling Lee received his Ph.D. degree from Department of Electrophysics, National Chiao Tung University, Taiwan in 2008. Now he is a postdoctoral researcher in National Tsing Hua University, Taiwan. His research interests include the synthesis of low dimensional materials, the optical and electrical characterizations, and the discovery of crystallographic characteristics using synchrotron radiation.

Chiou-Ru Cheng received her B.S. degree in Quantitative Finance and Material Science and Engineering, National Tsing Hua University and M.S. degree in Electrical Engineering, National Cheng Kung University. Currently, working as a Yield Excellence Engineer in TSMC.

Yi-Jen Yu is technician of instrument center, National Tsing Hua University, Taiwan.

Yuanfei Ai is currently an assistant professor at Dongguan University of Technology. His current scientific interests focus on the design and synthesis of three-dimensional nanostructures, and investigation of their fundamental properties and potential applications in flexible energy storage devices and integrated devices.

Johnny C. Ho is a professor of materials science and engineering at City University of Hong Kong. He received his BS degree in chemical engineering, and his MS and PhD degrees in materials science and engineering from the University of California, Berkeley, in 2002, 2005, and 2009, respectively. From 2009–2010, he was a postdoctoral research fellow in the Nanoscale Synthesis and Characterization Group at Lawrence Livermore National Laboratory. His research interests focus on synthesis, characterization, integration, and device applications of nanoscale materials for various technological applications, including nanoelectronics, sensors, and energy harvesting. Details can be found at: https://hocityu.com/about_pi.html

Yu-Lun Chueh is a distinguished professor in Department of Materials Science and Engineering, National Tsing Hua University, Taiwan. His research directions include (1) Direct growth, fundamental characterizations, and optoelectronic applications of two-dimensional materials, including graphene and transition metal dichalcogenide. (2) Energy harvesting by Cu(In,Ga)Se$_2$ solar cells and phase-changed molten salts. (3) Low power resistive random access memory. Details can be found at: http://nanoscienceandnanodevicelab.weebly.com/index.html.